Dispersive spherical optical model of neutron scattering from ^{27}Al up to 250 MeV

A. Molina,[1,*] R. Capote,[1,2,†] J. M. Quesada,[1,‡] and M. Lozano[1,§]
[1]*Departamento de Física Atómica, Molecular y Nuclear, Universidad de Sevilla, Facultad de Física, AP 1065, E-41080 Sevilla, Spain*
[2]*Centro de Estudios Aplicados al Desarrollo Nuclear, AP 100, Miramar, La Habana, Cuba*
(Received 14 November 2001; published 4 March 2002)

A spherical optical model potential (OMP) containing a dispersive term is used to fit the available experimental database of $\sigma(\theta)$ and σ_T for $n+^{27}$Al covering the energy range 0.1–250 MeV using relativistic kinematics and a relativistic extension of the Schrödinger equation. A dispersive OMP with parameters that show a smooth energy dependence and an energy-independent geometry are determined from fits to the entire data set. A very good overall agreement between experimental data and predictions is achieved up to 150 MeV. Inclusion of nonlocality effects in the absorptive volume potential allows one to achieve an excellent agreement up to 250 MeV.

DOI: 10.1103/PhysRevC.65.034616 PACS number(s): 11.55.Fv, 24.10.Ht

I. INTRODUCTION

During the last 15 years, a great deal of theoretical attention has been devoted to achieving a proper formulation of the nuclear mean field at positive and negative energies. A significant contribution to the solution of this problem can be considered the work of Mahaux and co-workers on dispersive optical-model analysis [1–5]. A unified description of a nuclear mean field in a dispersive optical model is accomplished by using a dispersion relation, which links the real and absorptive terms of the optical model potential (OMP). The dispersive optical model (DOM) provides a natural extension of the optical-model-derived data into the bound-state region. In this way a physically self-consistent description of the energy dependence of the OMP is obtained, and a prediction of single-particle, bound-state quantities using the same potential at negative energies becomes possible. Moreover, an additional constraint imposed by dispersion relations helps to reduce the ambiguities in deriving phenomenological OMP parameters from the experimental data.

A dispersive OMP analysis was applied to nucleus-nucleus systems [6–9], where the energy dependence of the real central potential at low energies near the Coulomb barrier was studied, and contributions of the dispersion terms evaluated. However, for a nucleus-nucleus system, the dispersive OMP analysis is limited to the positive energy region, because it is not yet clear how to deal with particle clusters bound in a nucleus. Some progress has been achieved in applications of the dispersive OMP analysis to the alpha-nucleus scattering, improving our knowledge of the alpha cluster effective interaction inside a nuclear system [10]. Pionering works on dispersive OMP analysis for nucleon scattering were made by Passatore [11] and Lipperheide and Schmidt [12]. A great success was achieved in deriving DOM potentials for nucleon scattering on closed-shell nuclei like ^{40}Ca [4,13–16], ^{90}Zr [16–20], and ^{208}Pb [1–4,13,14,21,22], for which experimental information on bound states is available. Many studies also dealt with neutron scattering on nonmagic nuclei (^{39}K [23], ^{51}V [24], ^{86}Kr [25], ^{89}Y [26], ^{93}Nb [27], ^{113}In [28], and ^{209}Bi [22,29,30]). However, very few studies were devoted to DOM potentials for nuclei with $A \lesssim 30$. Only one preliminary DOM analysis was reported for ^{27}Al(n,n) [31]. There are two publications making a DOM analysis for proton-induced reactions on aluminum up to 60 MeV [32,33].

The main purpose of this contribution is to construct a complex mean field ''felt'' by neutrons in ^{27}Al theoretically valid from -50 up to 250 MeV energy. There exist two main versions of the dispersion relation approach. In both methods, the real and imaginary parts of the mean field are connected by a dispersion relation; moreover, a mean field is required to reproduce the experimental value of the Fermi energy E_F closely. The main difference between the two methods is the following: (i) In the ''variational moment approach'' [13,14], the parameters of the complex mean field are determined by fitting radial moments of phenomenological optical-model potentials. (ii) In the ''dispersive optical model analysis'' [15–17], the unknown parameters are derived by performing optical-model fits to experimental scattering cross sections that need to be available over as broad an energy range as possible.

In the present work a variation of the dispersive optical model analysis is applied to a determination of the nuclear mean field for a neutron-^{27}Al system. An Ohio University–Los Alamos collaboration published an extensive survey of neutron-nucleus total cross-section measurements up to 600 MeV [34,35]. These high precision data, together with earlier neutron differential scattering data available in the interval 1–26 MeV, form the database considered at positive energies. The Fermi energy value derived from nuclear masses is used to constrain the mean-field value at negative energies. Therefore, the energy variation of the model parameters is reasonably defined over a wide range, an extremely important point for a successful dispersive analysis. It is remarkable that our total-cross section database goes up to the region where surface absorption can be safely neglected. Since the employed database extends up to 250 MeV, and since the recent σ_T data are very accurate, i.e., the uncertainty $\Delta\sigma_T$ is

*Email address: alberto@nucle.us.es
†Email address: rcapotenoy@yahoo.com
‡Email address: quesada@us.es
§Email address: lozano@us.es

about $\pm 1\%$, we use relativistic kinematics and a relativistic equation equivalent to the Schrödinger equation in all our calculations.

Other motivation for our work is that aluminum is an important structural material for accelerator-driven systems, and its cross sections are often used as references to determine other cross sections [36]. There exist phenomenological OMP's (in the sense that dispersive relations constrain is not used) describing neutron scattering on aluminum up to high incident energy. The LANL high energy evaluation of Chadwick *et al.* [37] employed the OMP of Petler *et al.* [38] up to 60 MeV and the Madland global OMP [39] from 60 up to 150 MeV. Lee *et al.* [40] derived a phenomenological OMP which described neutron scattering from ^{27}Al up to 250 MeV incident energy. Recently a global phenomenological parametrization valid from 1 keV to 200 MeV for $A \geqslant 27$ nuclei was proposed by Koning and Delaroche [41].

Usually in DOM analysis the absorptive potentials are considered symmetric about the Fermi energy E_F, and nonzero in the energy gap surrounding E_F. However, Mahaux and Sartor [4] pointed out that (i) due to nonlocality effects, the absorptive potential will be highly asymmetric(with respect to E_F); and (ii) there should be an energy gap centered about E_F in which the absorption term drops to zero, at least for energies between the first-hole and first-particle states. A recent DOM analysis of neutron scattering on ^{208}Pb and ^{209}Bi [22] failed to describe σ_T data for energies above 40 MeV using an asymmetric version of the absorptive potentials for large positive and large negative energies. We will present strong evidence to favor asymmetric absorptive potentials for a proper description of the neutron-scattering σ_T data for energies between 150 and 250 MeV.

The paper is structured as follows. Section II provides a description of the dispersive optical model formalism, the solved wave equation, and the forms of the energy and radial dependencies of the real, imaginary, and spin-orbit potentials. Section III describes the compound nucleus (CN) calculations, the ^{27}Al(n,n) experimental database, our procedure for searching, and the resulting relativistic and nonrelativistic spherical DOM potentials for ^{27}Al(n,n). In the same section we compare derived DOM potentials with phenomenological potentials and experimental data. Finally, Sec. IV contains our conclusions.

II. DOM FORMALISM

A. Optical-model potential and wave equation

The optical-model analysis was carried out with a semirelativistic generalization of the conventional nonrelativistic Schrödinger formulation of the scattering process [42]. Relativistic kinematics was used for the projectile, but it was assumed that the target motion in the center-of-mass system could be treated nonrelativistically. A relativistic equivalent to the Schrödinger equation was generated by appropriate reduction of the Dirac equation for a massive, energetic fermion (mass m and c.m. wave number k) moving in a localized central potential $V(r)$ taken as the time-like component of a Lorentz four-vector. In a reduced two-body problem with a relativistic projectile but a nonrelativistic target (mass M), the large component of the partial wave function $F_l(\rho)$ can be shown to satisfy the radial equation

$$\left\{ \frac{d^2}{d\rho^2} + \left[1 - \frac{V(\rho)}{T_c} - \frac{l(l+1)}{\rho^2} \right] \right\} F_l(\rho) = 0, \tag{1}$$

where $\rho = kr$, T_c is the total c.m. kinetic energy, l is the orbital angular momentum, and $V(\rho)$ is the renormalized nuclear optical potential:

$$V(\rho) = \gamma U(r), \quad \gamma = 1 + \frac{T_c}{T_c + 2m}. \tag{2}$$

Equation (1) is formally identical to the radial equation for the solution of the nonrelativistic Schrödinger equation for an analogous scattering problem with a nuclear potential renormalized by a factor γ. This factor becomes increasingly important as the projectile kinetic energy increases [see Eq. (2)], leading to an effective increase of the potential depth. The spin-orbit term in $V(r)$ employed in this analysis is a purely phenomenological one, since the intrinsic spin-orbit term in the Dirac equation is negligibly small in the above limits. Equation (1) was used in all calculations. In a nonrelativistic case, we set the factor γ equal to 1 and nonrelativistic kinematics was employed; otherwise relativistic kinematics and the factor γ according to Eq. (2) were used.

Our analysis spans an energy range from 0.1 to 250 MeV. Both direct and statistical processes contribute to nucleon-nucleus elastic scattering at these energies. According to our estimation, the statistical processes are important up to 12 MeV in aluminum. A compound nucleus calculation will be described in Sec. III C. The direct processes, increasingly dominant at higher energies, can be described by the optical model. Although the ^{27}Al nucleus is deformed, the spherical OMP was applied successfully [38,40,43]. An *a posteriori* analysis of the impact of this approximation on the calculated observables will be discussed below.

The optical model potential may be written as

$$\begin{aligned} U(r,E) = &-[V_v(E) + iW_v(E)] f_{WS}(r,R_v,a_v) - [V_s(E) \\ &+ iW_s(E)] g_{WS}(r,R_s,a_s) + \left(\frac{\hbar}{m_\pi c} \right)^2 [V_{so}(E) \\ &+ iW_{so}(E)] \frac{1}{r} \frac{d}{dr} f_{WS}(r,R_{so},a_{so}) (\vec{l} \cdot \vec{\sigma}), \end{aligned} \tag{3}$$

where the successive complex-valued terms are the volume central, surface central, and spin-orbit potentials. The volume shape $f_{WS}(r,R_v,a_v)$ is a standard Woods-Saxon form factor specified by a potential radius R_v and diffuseness a_v. The surface shape is the first derivative of the Woods-Saxon form specified by a potential radius R_s and diffuseness a_s:

$$g_{WS}(r,R_s,a_s) = -4a_s \frac{d}{dr} f_{WS}(r,R_s,a_s). \tag{4}$$

The reduced radius parameter r_i is introduced as usual by the relation $R_i = r_i A^{1/3}$. In our formulation of the OMP in Eq. (3), the real and imaginary central volume terms share the same geometry parameters r_v and a_v, and likewise the real and imaginary central surface terms share the same r_s and a_s. This assumption [3] can be seen as a consequence of the dispersive relations, allowing us to reduce the number of geometrical parameters in the OMP.

For the spin-orbit potential we adopt the parameters obtained by Koning *et al.* [36], namely,

$$V_{so}(E) = 6.0 \exp(-0.005E) \ \text{MeV},$$

$$W_{so}(E) = 0.2 - 0.011E \ \text{MeV},$$

$$r_{so} = 1.017 \ \text{fm}, \quad a_{so} = 0.6 \ \text{fm}. \tag{5}$$

In a dispersion relation treatment, the real central potential strength consists of a term which varies slowly with energy, the so called Hartree-Fock (HF) term $V_{HF}(E)$, plus a correction term $\triangle V(E)$ which is calculated using a dispersion relation. The depth of the dispersive term of the potential $\triangle V(E)$ can be written in the subtracted form

$$\triangle V(E) = \frac{\mathcal{P}}{\pi} \int_{-\infty}^{\infty} W(E') \left(\frac{1}{E'-E} - \frac{1}{E'-E_F} \right) dE'. \tag{6}$$

With the assumption that $W(E)$ be symmetric with respect to the Fermi energy E_F, Eq. (6) can be expressed in a form which is stable under numerical treatment [17], namely,

$$\triangle V(E) = \frac{2}{\pi}(E-E_F) \int_{E_F}^{\infty} \frac{W(E') - W(E)}{(E'-E_F)^2 - (E-E_F)^2} dE', \tag{7}$$

where $W(E)$ is the imaginary part of the OMP. The dispersive term $\triangle V(E)$ is divided into two terms $\triangle V_v(E)$ and $\triangle V_s(E)$, which arise through dispersion relations (7) from the volume $W_v(E)$ and surface $W_s(E)$ imaginary potentials, respectively. If the imaginary potential geometry is energy dependent, then the radial dependence of the dispersive correction cannot be expressed using a Wood-Saxon form factor, i.e., $\triangle V_v(r,E) \neq \triangle V(E) f(r,R,a)$. However, to simplify the problem, the OMP geometry parameters used in this work are energy independent. In this case, using the definitions of Eq. (3), the real volume $V_v(E)$ and surface $V_s(E)$ central part of the DOM potential are given by

$$V_v(E) = V_{HF}(E) + \triangle V_v(E),$$

$$V_s(E) = \triangle V_s(E). \tag{8}$$

It is known that the energy dependence of the depth $V_{HF}(E)$ is due to the replacement of a microscopic nonlocal HF potential by a local equivalent. For a Gaussian nonlocality, $V_{HF}(E)$ is a linear function of E for large negative E, and is an exponential for large positive E. Following Mahaux and Sartor [4], the energy dependence of the Hartree-Fock part of the nuclear mean field is taken as that found by Lipperheide [44],

$$V_{HF}(E) = V_0 \exp[-\alpha_{HF}(E-E_F)], \tag{9}$$

where the parameters V_0 and α_{HF} are undetermined constants. Equation (9) can be used to describe HF potential in the scattering regime [4].

It is useful to represent the variation of surface $W_s(E)$ and volume absorption potential $W_v(E)$ depth with energy in functional forms suitable for the dispersive optical model analysis. An energy dependence for the imaginary volume term has been suggested in studies of nuclear matter theory [45],

$$W_v(E) = A_v \ \frac{(E-E_F)^n}{(E-E_F)^n + (B_v)^n}, \tag{10}$$

where A_v and B_v are undetermined constants. Following Mahaux and Sartor [2], we adopt $n=4$. An energy dependence for the imaginary-surface term was suggested by Delaroche *et al.* [17] to be

$$W_s(E) = A_s \ \frac{(E-E_F)^m}{(E-E_F)^m + (B_s)^m} \ \exp(-C_s|E-E_F|), \tag{11}$$

where $m=4$ and A_s, B_s, and C_s are undetermined constants.

According to Eqs. (10) and (11), the imaginary part of the OMP is assumed to be zero at $E=E_F$, and nonzero everywhere else. A more realistic parametrization of $W_v(E)$ and $W_s(E)$ forces these terms to be zero in some region around the Fermi energy. A physically reasonable energy for defining such a region is the average energy of the single-particle states E_p [4]. For aluminum we used a value $E_p = -5.66$ MeV, obtained by averaging the first three particle states reported in the microscopical single-particle level calculation by Moller and Nix [46]. The experimental value of the Fermi energy E_F, derived from mass differences, is equal to -10.392 MeV.

Therefore, a definition for imaginary part of the OMP can be written as

$$W_v(E) = \begin{cases} 0 & \text{for } E_F < E < E_p \\ A_v \ \dfrac{(E-E_p)^n}{(E-E_p)^n + (B_v)^n} & \text{for } E_p < E, \end{cases} \tag{12}$$

and likewise for surface absorption:

$$W_s(E)=\begin{cases} 0 & \text{for} \quad E_F<E<E_p \\ A_s \ \dfrac{(E-E_p)^m}{(E-E_p)^m+(B_s)^m} \ \exp(-C_s|E-E_P|) & \text{for} \quad E_p<E. \end{cases} \tag{13}$$

The symmetry condition

$$W(2E_F-E)=W(E) \tag{14}$$

is used to define imaginary part of the OMP for energies below the Fermi energy. Equations (12) and (13) are used to describe the imaginary absorptive potential in this contribution.

B. High-energy behavior of the volume absorption

The assumption that the imaginary potential $W_v(E)$ is symmetric about $E'=E_F$ [according to Eq. (14)] is plausible for small values of $|E'-E_F|$; however, as pointed out by Mahaux and Sartor [4] this approximate symmetry no longer holds for large values of $|E'-E_F|$. In fact the influence of the nonlocality of the imaginary part of the microscopic mean field will produce an increase of the empirical imaginary part $W(r,E')$ at large positive E', and approaches zero at large negative E' [1,47]. Following Mahaux and Sartor [4], we assume that the absorption strengths are not modified below some fixed energy E_a. They used $E_a=60$ MeV; however, this value is fairly arbitrary [4]. Let us assume the nonlocal imaginary potential to be used in the dispersive integral is denoted by $\tilde{W}_v(E)$; then we can write [5]

$$\tilde{W}_v(E)=W_v(E)\left[1-\frac{(E_F-E-E_a)^2}{(E_F-E-E_a)^2+E_a^2}\right],$$

$$\text{for} \quad E<E_F-E_a \tag{15}$$

and

$$\tilde{W}_v(E)=W_v(E)+\alpha\left[\sqrt{E}+\frac{(E_F+E_a)^{3/2}}{2E}-\frac{3}{2}\sqrt{(E_F+E_a)}\right], \quad \text{for} \quad E>E_F+E_a. \tag{16}$$

These functional forms are chosen in such a way that the function and its first derivative are continuous. At large positive energies nucleons ''sense'' the ''hard core'' repulsive region of the nucleon-nucleon interaction, and $\tilde{W}_v(E)$ diverges like $\alpha\sqrt{E}$. Using a model of a dilute Fermi gas hard sphere, the coefficient α can be estimated to be equal to 1.65 $\text{MeV}^{1/2}$ [47], assuming that the Fermi impulse k_F is equal to 1.36 fm^{-1} and the radius of the repulsive hard core is equal to 0.4 fm. Conversely, at large negative energies the volume absorption decreases and goes asymptotically to zero. The nonlocal imaginary absorption potential $\tilde{W}_v(E)$ and the symmetric imaginary absorption potential $W(E)$ are represented by solid and dotted lines, respectively, in the lower panel of Fig. 1.

The asymmetric form of the volume imaginary potential of Eqs. (15) and (16) results in a dispersion relation that must be calculated directly from Eq. (6), and separates into three additive terms [48]. Therefore, we write the dispersive correction in the form

$$\triangle\tilde{V}_v(E)=\triangle V_v(E)+\triangle V_<(E)+\triangle V_>(E), \tag{17}$$

where $\triangle V_v(E)$ is the dispersive correction due to the symmetric imaginary potential of Eq. (12), and the terms $\triangle V_<(E)$ and $\triangle V_>(E)$ are dispersive corrections due to the asymmetric terms of Eqs. (15) and (16), respectively. The resulting energy dependence of the dispersive integrals $\triangle\tilde{V}_v(E)$ and $\triangle V_v(E)$ for both the nonlocal imaginary absorption potential $\tilde{W}_v(E)$ and the symmetric imaginary absorption potential $W(E)$ is represented by solid and dotted lines, respectively, in the upper panel of Fig. 1. While the symmetric case features equal contributions coming from negative and positive energies, in the asymmetric case the negative-energy contribution to the dispersive integral is very different from the positive-energy value. The resulting dispersive correction for the asymmetric case starts to increase for energies above 50 MeV, making a significant contribution to the real part of the OMP.

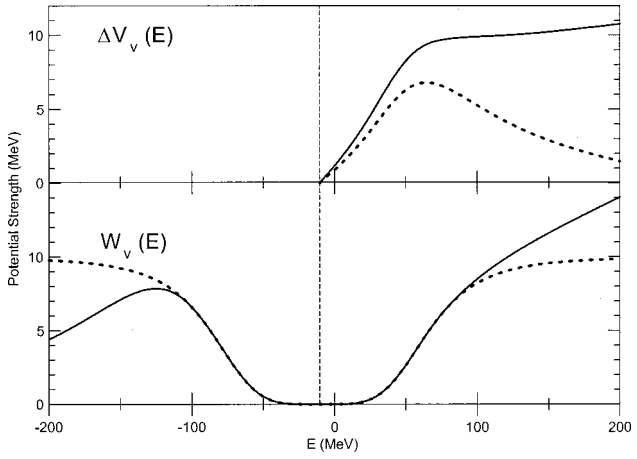

FIG. 1. Dependence upon energy of the dispersive volume contribution of the real central potential of the $n+{}^{27}\text{Al}$ mean field. The dotted curve corresponds to Eq. (12), in which it is assumed that the imaginary part is symmetric about the Fermi energy. The thick solid curves correspond to the asymmetric model, considering the nonlocal behavior of the imaginary volume absorption above certain energy E_a following Eqs. (15) and (16). The thin dashed line corresponds to the Fermi energy.

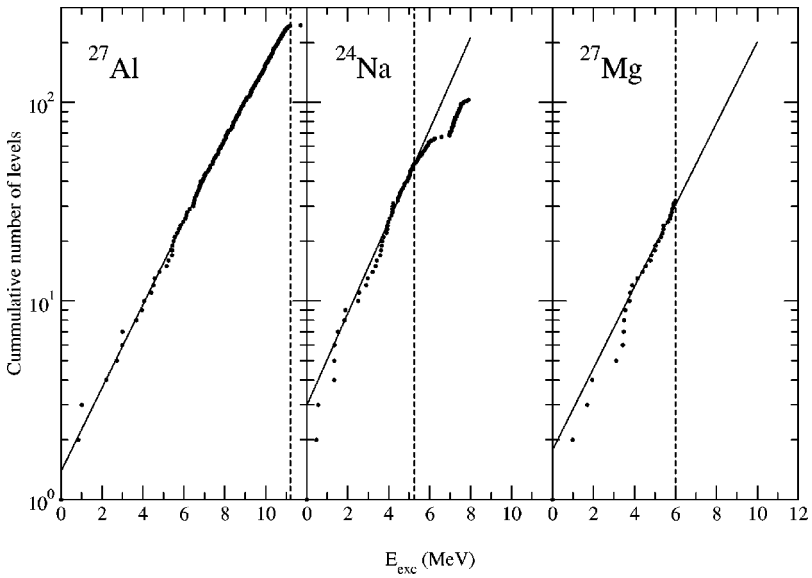

FIG. 2. Cumulative number of levels as a function of the excitation energy for the three residual nuclei considered in the CN cross-section calculations. The discrete level data are from the RIPL [46] and are well represented by the ''constant temperature'' level density formula of Ref. [81] using parameters from Table I. The cutoff energy is indicated by the vertical dashed line. Above the cutoff energy the ''constant temperature'' level density formula was used.

It should be noted that nonlocality corrections [Eqs. (15) and (16)] can be used either for the volume or surface imaginary potential; however, Mahaux and Sartor [4] showed that the nonlocality consideration for the surface imaginary potential has a very small effect on the calculated cross sections. Therefore, in this work we followed Ref. [5] and only considered the effects of nonlocality in the volume absorption.

III. DISPERSIVE OPTICAL MODEL ANALYSIS

A. DOM software

Search optical model codes ECIS95 in the external input mode [49,50] and COH v 2.2 [51] were used for DOM analyses using relativistic and nonrelativistic kinematics respectively. A modification was introduced into the latter code to force equality of the real and imaginary surface (volume) geometry parameters $R_s, a_s (R_v, a_v)$ during the search procedure, as is implicit in Eq. (3). The code does not include the dispersion relations; therefore, the dispersion integrals (7) of the symmetric forms (12) and (13) of the imaginary potential were calculated numerically using a Gauss quadrature method [52], while the asymmetric contribution was calculated analytically [see Eqs. (16)–(19) of Ref. [48]]. An auxiliary code system was developed to produce proper input data sets for both optical model codes, and to calculate for each data set (i.e., for each energy) the χ^2 quantity according to

$$\chi^2(E) = \sum_{i=1}^{N_\sigma} \left[\frac{\sigma_{\rm expt}(E,\theta_i) - \sigma_{calc}(E,\theta_i)}{\Delta\sigma_{\rm expt}(E,\theta_i)} \right]^2 + \left[\frac{\sigma^{tot}_{\rm expt}(E) - \sigma^{tot}_{calc}(E)}{\Delta\sigma^{tot}_{\rm expt}(E)} \right]^2 . \quad (18)$$

Here, $\sigma_{calc}(E,\theta_i)$ $[\sigma^{tot}_{calc}(E)]$ and $\sigma_{\rm expt}(E,\theta_i)$ $[\sigma^{tot}_{\rm expt}(E)]$, are the differential (total) cross sections from the optical model calculations and experiments for a given laboratory energy E, respectively, and $\Delta\sigma_{\rm expt}(E,\theta_i)[\Delta\sigma^{tot}_{\rm expt}(E)]$ is the experimental uncertainty reported. The N_σ is the number of data points for $\sigma_{\rm expt}(E,\theta_i)$. Our code system allows us to fine tune the OMP parameters of interest to minimize the total search χ^2 of the entire data set.

B. Summary of the experimental databases

A survey of the experimental data spanning from 0.1 to 250 MeV used in the DOM analyses is presented in this section. The ^{27}Al(n,n) $\sigma(\theta)$ data were obtained from Towle and Gilboy [53] at 1, 2, 3, and 4 MeV; Tanaka *et al.* [54] at 4.8, 6, 7, and 8 MeV; Kinney and Perey [55] at 5.4, 6.4, 7.5, and 8.6 MeV; Dagge *et al.* [56] at 7.62 MeV; Velkley *et al.* [57] at 9 MeV; Boerker *et al.* [58] at 10.2 MeV; Whisnant *et al.* [43] at 11, 14, and 17 MeV; Petler *et al.* [38] at 18, 20, 22, 25, and 26 MeV; Bratenahl *et al.* [59] at 84 MeV; Salmon [60] at 96 MeV; and Van Zyl *et al.* [61] at 136 MeV. The ^{27}Al(n,n) $A_y(\theta)$ data were obtained from Dagge *et al.* [56] at 7.62 MeV and Martin and Walter [62] at 14 and 17 MeV. These polarization data were used only for testing spin-orbit interaction. Energy-averaged total cross sections σ_T for ^{27}Al were obtained from Finlay and co-workers [34,35] from 5.3 to 250 MeV. Additional energy-averaged σ_T data were taken from Refs. [63–74] to be used for comparing predictions of the model. We selected measurements containing several points in energy, specially, all with data above 20 MeV. In examining all the available experimental total cross-section data, the high-resolution cross-section data of Ref. [75] were found to be inconsistent with the rest of the dataset, and were ignored in our analysis.

C. Compound-nucleus corrections

The statistical model of nuclear reaction according to the Hauser-Feshbach theory [76], with width fluctuation corrections as modified by Moldauer [77], is used to compute the CN contributions to the elastic channel. When the cross section is averaged over many CN resonances, the shape elastic differential cross section can be incoherently added to the

TABLE I. Constant temperature level density parameters for residual nuclei in an $n+^{27}$Al reaction.

Residual nucleus	E_{cut} (MeV)	T (MeV)	E_0 (MeV)
^{27}Al	11.2	2.071	−0.678
^{24}Na	5.2	1.875	−2.046
^{27}Mg	6.0	2.113	−1.2157

compound elastic contribution to compare with the experimentally observed elastic-scattering cross section. For neutron energies larger than 12 MeV, the compound-elastic contribution can be neglected. The CN cross-section calculation is built-in inside the search code COH [51]. Three reaction channels are considered in the statistical-model calculations of the ^{28}Al CN decay: (n,n), (n,p), and (n,α). Transmission coefficients for proton and alpha emission in the exit channels were calculated from the spherical OMP parameters by Perey [78] and Arthur and Young [79] (a modification of Lemos OMP [80]), respectively. The transmission coefficients in the entrance and inelastic channels were calculated using the DOM potential of the present work.

Discrete level information is used to represent low-lying states, and the Gilbert-Cameron level density formula [81] is used to represent the high-lying continuum of states. Figure 2 shows the cumulative number of levels as a function of excitation energy for the residual nuclei of the three reaction channels. The discrete state data are taken from the Belgya compilation contained in RIPL [46]. The vertical lines indicate the cutoff energy between the discrete states and the continuum. It is well known that a CN calculation is highly sensitive to the level density parameters modeling the continuum of the excited states. We used a ''constant temperature'' formula [81] to estimate the total number of excited states available at excitation energy E, $N(E)=\exp[(E-E_0)/T]$, where T is the ''nuclear temperature'' and E_0 is the energy shift. These two parameters are determined by fitting the cumulative number of available experimental states up to some cutoff energy. The level density parameters for all three residual nuclei involved in CN cross-section calculations are listed in Table I. A cumulative number of levels, as calculated by the ''constant temperature'' model using these parameters, is shown by solid lines in Fig. 2.

D. Search procedure

It is well known that the search routine does not always converge to the optimum solution, especially when we are dealing with strongly correlated OMP parameters. In our DOM analysis we performed a global χ^2 optimization combined with a grid search using a χ^2 fit in a limited energy region, using a maximum number of two fitting parameters simultaneously. Our search procedure can be divided in four main steps.

(1) The search for an imaginary $W_v^{emp}(E)$ empirical potential depth using total cross-section data between 70 and 150 MeV, neglecting real and imaginary surface contributions. This energy range is selected in order to neglect the surface absorptive potential in the first iteration. Once empirical values $W_v^{emp}(E)$ are obtained, a fit of the absorptive volume potential $W_v(E)$ using Eq. (12) is carried out. In this way volume absorption is fixed, as well as the dispersive volume contribution $\triangle V_v(E)$ to the central real potential, which is calculated by integration. The empirical values of the real volume potential depth $V_v^{emp}(E)$, combined with $\triangle V_v(E)$, are used to obtain a set of empirical points corresponding to $V_{HF}^{emp}(E)$. A typical set of empirical values derived in the above described way can be seen in Fig. 3, as obtained with the search code COH. Finally Eq. (9) is used to obtain the V_0 and α_{HF} parameters that offer a best fit to the

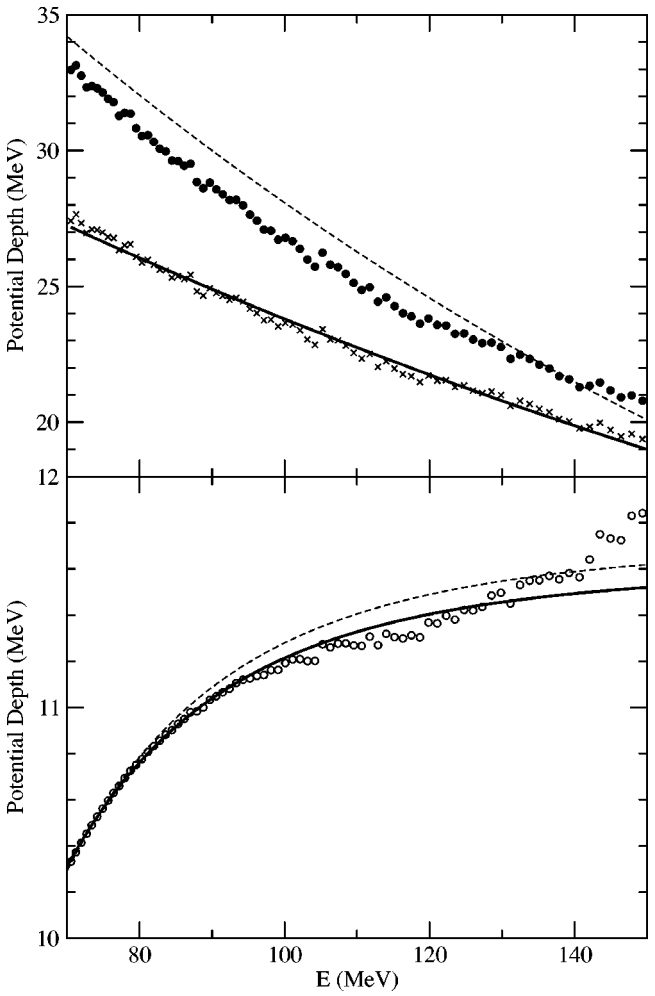

FIG. 3. Empirical real volume (solid circles) and imaginary volume potential depth (empty circles) of the OMP for $n+^{27}$Al as determined from individual best χ^2 fit searches using σ_{tot} data in the interval $70<E<150$ MeV after the first iteration. Upper panel: the solid line for the Hartree-Fock potential is the functional representation defined in Eq. (9). The dashed line denotes the starting guess values calculated using the OMP of Ref. [40]. The crosses represent the empirical values of the Hartree-Fock-type potential obtained after the dispersive contribution coming from the volume imaginary part of the OMP was subtracted from the real volume empirical values. Lower panel: the solid line for the absorptive potential is the functional representation defined in Eq. (12). The dashed line denotes the starting guess values calculated using the OMP of Ref. [40].

empirical real potential data. In the fitting process the strength V_0 was constrained for the DOM predicted first-particle and first-hole states to be centered around the experimental value of the Fermi energy.

(2) At each energy for which neutron elastic differential cross-section data and neutron total cross-section data are available from 1 to 26 MeV, we have conducted a best χ^2 fit by searching in volume real $V_v^{emp}(E)$ and surface imaginary $W_s^{emp}(E)$ empirical potential depths. In the first iteration the corresponding dispersive surface contribution $\triangle V_s(E)$ to the central real potential was calculated by integration from the starting OMP parameters. CN contributions and width fluctuation corrections were considered in all calculations for an incident energy below 12 MeV. Once empirical values $W_s^{emp}(E)$ are obtained, a fit of the absorptive surface-peaked potential $W_s(E)$ using Eq. (13) is carried out. The dispersive surface contribution $\triangle V_s(E)$ to the central real potential is re-evaluated by integration. The empirical values of the real volume potential depth $V_v^{emp}(E)$, combined with the $\triangle V_v(E)$ calculated for these energies, are used to increase the set of empirical points corresponding to $V_{HF}^{emp}(E)$. Equation (9) is used to refine the fitting of the V_0 and α_{HF} parameters, derived in point (1), using the whole empirical set of potential values obtained in steps (1) and (2). We iterate over steps (1) and (2) until the empirical potential strengths are consistent with our predefined energy functional [see Eqs. (9), (13), and (12)] over the whole energy range.

(3) After fixing potential strengths, the optimum geometry parameters were searched for, iterating over steps (1) and (2) to redefine the potential strengths corresponding to the optimized geometry parameters.

(4) Finally, a global χ^2 optimization using the whole experimental database was carried out to obtain the minimum in the χ^2 multiparameter surface.

E. ^{27}Al(n,n) DOM analysis

We started our analysis by using a nonrelativistic formulation to fit the experimental data. Initial values for geometrical parameters were provided by the energy-independent geometry deduced by Whisnant *et al.* [43] and used by Petler *et al.* [38] for a phenomenological analysis of the data up to 26 MeV. They found $r_v = 1.18$ fm, $a_v = 0.64$ fm, $r_s = 1.26$ fm, and $a_s = 0.58$ fm. Because the general form of the energy dependence of the imaginary potential used in the present model is similar to the ^{27}Al(n,n) phenomenological OMP of Lee *et al.* [40], we used their real volume and imaginary potential parameters as a starting point for our analysis. We used symmetric imaginary absorptive potentials according to Eqs. (13) and (12); therefore, we adjusted seven parameters, namely, (V_0, α_{HF}), which define the smooth energy dependence of the real volume potential, and (A_v, B_v) and (A_s, B_s, C_s) defining the volume and surface absorptive potentials, respectively. After proper values were obtained by this global minimization, the energy-independent geometry parameters were also optimized. The derived nonrelativistic DOM potential parameters are listed in Table II.

TABLE II. Optical model parameters for the nonrelativistic dispersive potential for an $n + ^{27}$Al reaction up to 150 MeV.

Parameter (Unit)	Value
V_0 (MeV)	52.24
α_{HF} (MeV^{-1})	0.0071
A_v (MeV)	12.5
B_v (MeV)	58.8
r_v (fm)	1.20
a_v (fm)	0.65
A_s (MeV)	12.6
B_s (MeV)	3.25
C_s (MeV^{-1})	0.0395
r_s (fm)	1.11
a_s (fm)	0.64
E_F (MeV)	-10.392
E_p (MeV)	-5.66

The final σ_T DOM fits using a nonrelativistic potential are compared to ^{27}Al(n,n) data in Fig. 4. It should be stressed that the experimental total cross-section data (except those

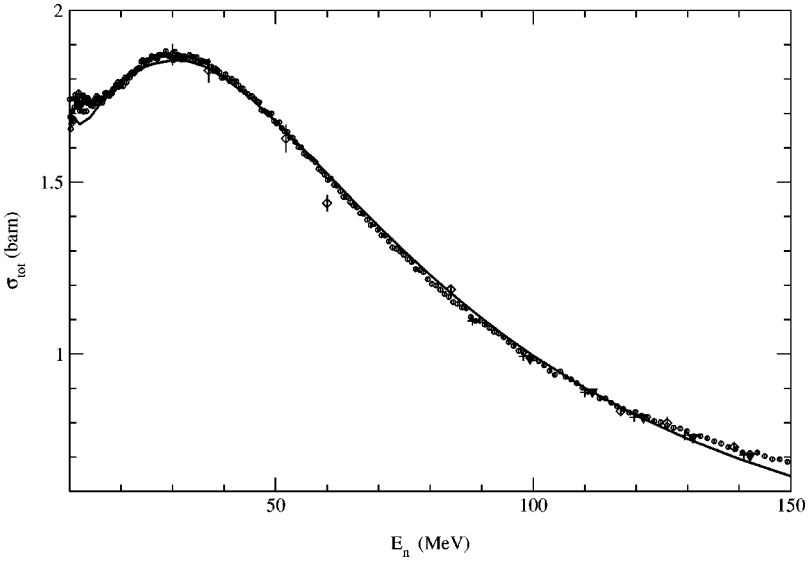

FIG. 4. Energy dependence of the $n + ^{27}$Al total cross section from 10 up to 150 MeV. The curve has been calculated using the nonrelativistic (solid line) DOM potential of the present work. Empty circles correspond to the experimental data of Refs. [34,35] used in the fitting procedure. The diamonds, crosses, and triangles are obtained from the measurements of Refs. [64], [66], and [67].

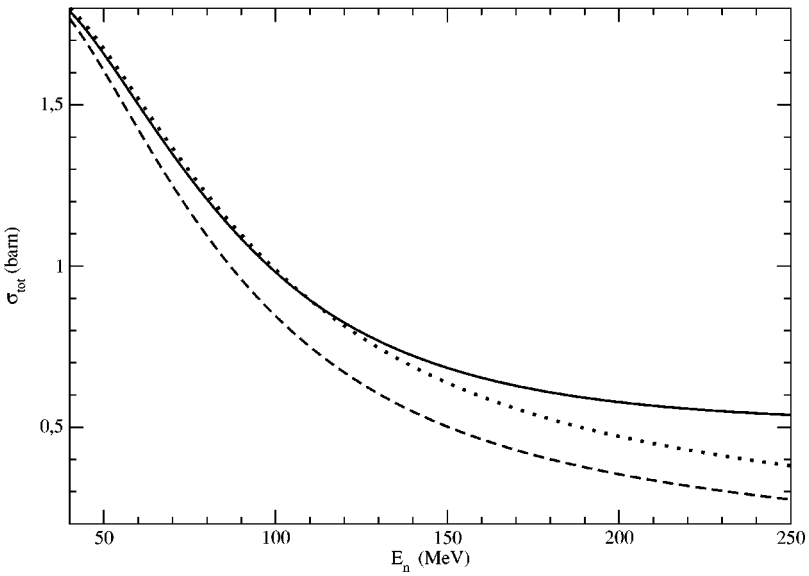

FIG. 5. Relativistic and nonlocality contribution to the total cross section. The total cross-section curves were calculated using the relativistic (solid line) and nonrelativistic (dotted line) DOM potentials of the present work. The dashed line denotes relativistic DOM potential results without nonlocality correction.

TABLE III. Optical model parameters for the relativistic dispersive potential for an $n+{}^{27}$Al reaction up to 250 MeV.

Parameter (Unit)	Value
V_0 (MeV)	53.5
α_{HF} (MeV^{-1})	0.0087
A_v (MeV)	7
B_v (MeV)	75
r_v (fm)	1.20
a_v (fm)	0.63
A_s (MeV)	12.5
B_s (MeV)	5
C_s (MeV^{-1})	0.034
r_s (fm)	1.11
a_s (fm)	0.64
E_F (MeV)	-10.392
E_p (MeV)	-5.66
E_a (MeV)	90.0

represented by the empty circles) shown in this figure were not used in the DOM parameter search. We can observe that the experimental total cross section at energies above 130 MeV was always underestimated by our nonrelativistic calculations. We cannot change the real volume potential depth (or the so-called Hartree-Fock potential) without spoiling the fits to the differential cross section. One solution could be to consider an increase of the radius of the real part of the OMP. However, this approach would obscure our treatment with an energy-independent geometry. Furthermore, it is theoretically obvious that relativistic effects and nonlocality should show up at this energy regime. Therefore, we decided to carry out a fully relativistic treatment, including nonlocal contributions to the absorptive potential, which will be reflected on the dispersive contribution to the real potential. The starting point in this second stage was the nonrelativistic DOM potential. We took into account the nonlocal contribution to the volume absorptive potential according to Eqs. (15) and (16). Only one additional parameter was included,

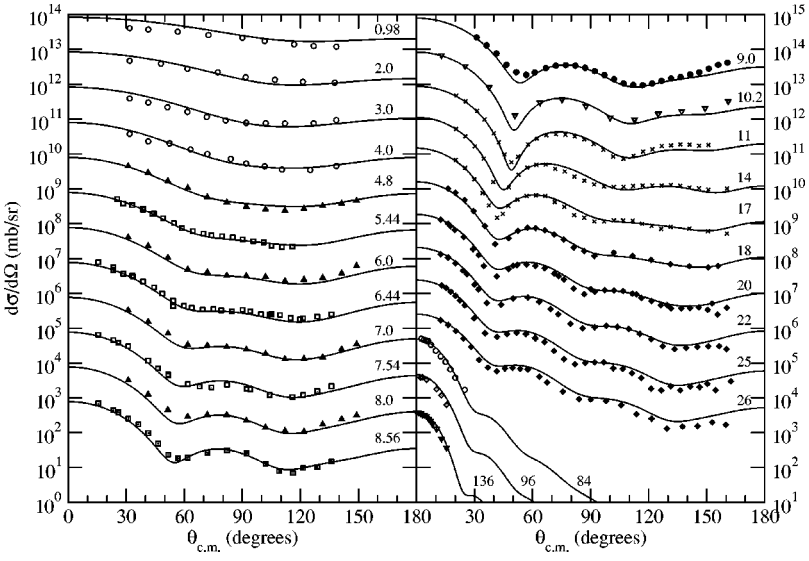

FIG. 6. Comparison between the neutron elastic differential cross-section experimental data and our DOM calculations (solid line). CN contributions were added to the direct reaction predictions for incident energies up to 12 MeV. The $\sigma(\theta)$ data were obtained from Ref. [53] at 1, 2, 3, and 4 MeV; Ref. [54] at 4.8, 6, 7, and 8 MeV; Ref. [55] at 5.4, 6.4, 7.5, and 8.6 MeV; Ref. [56] at 7.62 MeV; Ref. [57] at 9 MeV; Ref. [58] at 10.2 MeV; Ref. [43] at 11, 14, and 17 MeV; and Ref. [38] at 18, 20, 22, 25, and 26 MeV. It should be noted that data above 26 MeV was not used in the fitting process. The neutron incident energy is quoted above each calculated curve.

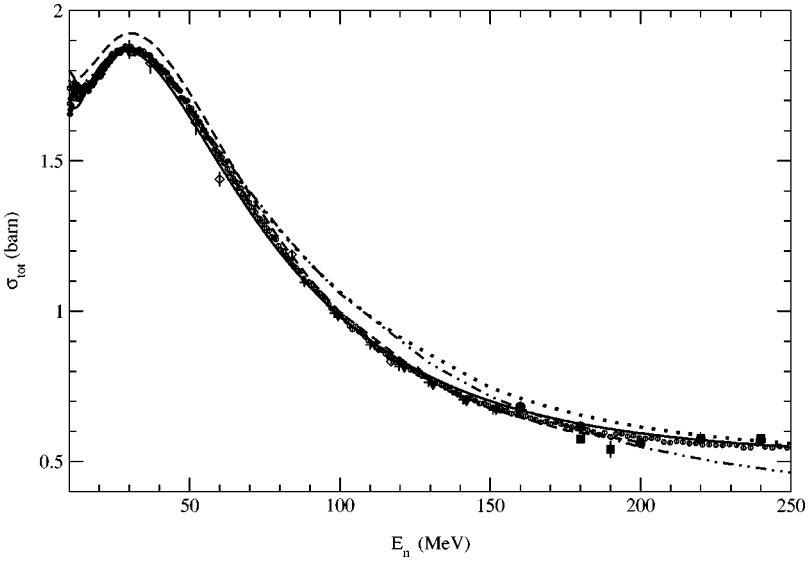

FIG. 7. Energy dependence of the $n+^{27}$Al total cross section above 10 MeV. The curves were calculated using the relativistic (solid line) DOM potential of the present work. The dotted, dot-dashed, and dashed lines were obtained from the phenomenological OMP of Refs. [39], [40], and [41], respectively, in their range of validity. Empty circles correspond to experimental data of Refs. [34,35] used in the fitting procedure. The diamonds, crosses, triangles, solid circles, and solid squares were from the measurements of Refs. [64], [66], [67], [72], and [63].

namely, the energy E_a, above which the nonlocal behavior of the volume absorptive potential is considered. In this latter χ^2 minimization the total cross-section data up to 250 MeV were included in the experimental database. All potential parameters changed because of the sizable contribution of the nonlocal absorption for energies above 40 MeV, as can be seen from Fig. 5. In the same figure the total cross-section calculated with the nonrelativistic DOM potential is shown for comparison. It is interesting to remark that the relativistic correction alone is clearly not enough for a correct description of the total cross section from 130 to 250 MeV. The final set of parameters of our dispersive relativistic optical model potential is summarized in Table III.

F. Comparison with the experimental cross section in the energy domain $0.1<E<250$ MeV

We now compare the experimental cross sections with those calculated from our DOM potentials. The geometrical parameters of the model and the strengths of the various components are specified in Tables II and III. The dispersion relations fully determine the dispersive contribution once the imaginary part of the mean field is specified.

The $\sigma(\theta)$ relativistic DOM fits are compared to ^{27}Al(n,n) data in Fig. 6. In general, the fits to $\sigma(\theta)$ are of high quality. A very good agreement between experimental data and calculations is observed in the energy region below 12 MeV, where the CN contribution is important. The highest deviation is observed for energies 25–26 MeV located near the diffraction maximum. In this energy region a difficulty was encountered during the fit process, evidenced by the fact that a *common* set of surface absorptive potential parameters giving acceptable fits to each type of data (differential and total cross section) could not be found. The fits to $\sigma(\theta)$ indicate smaller values of the imaginary surface potential depth A_S parameter, while fits to total cross section point to values larger by about 2 MeV. Experimental $\sigma(\theta)$ data for energies higher than 26 MeV were not included in the fitting procedure, but our relativistic DOM potential displays an

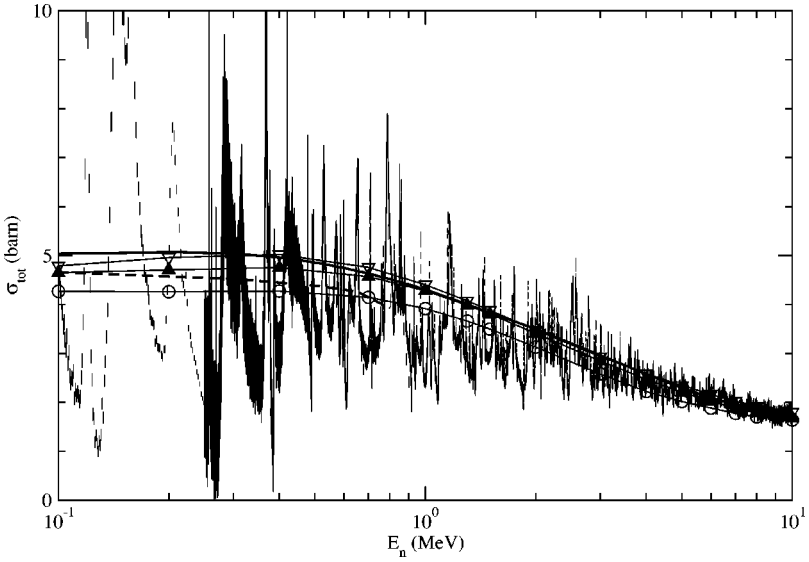

FIG. 8. Low-energy dependence of the $n+^{27}$Al total cross section from 0.1 up to 10 MeV. The curves have been calculated using the relativistic DOM potential without (solid line) and with (dashed line) reorientation effects. The circles, up triangles, and down triangles were obtained from the phenomenological OMP by Harper in Refs. [82], [38], and [41]. The high-resolution experimental data were obtained from measurements in Refs. [73] and [74].

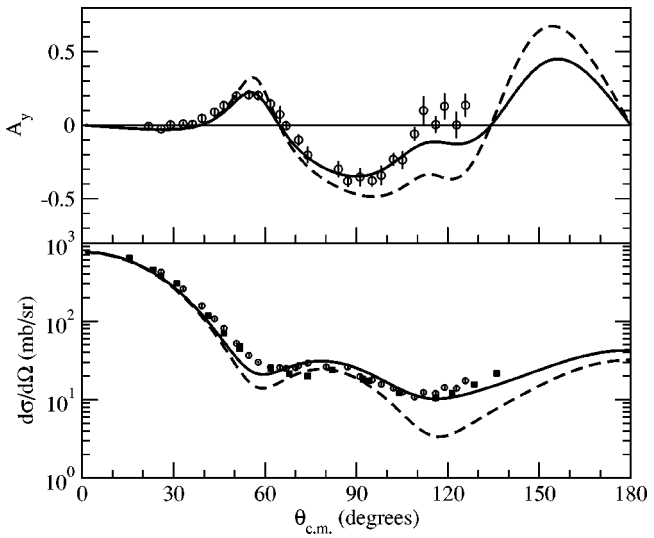

FIG. 9. The CN corrected $\sigma(\theta)$ and $A_y(\theta)$ data (solid line) at $E_n = 7.62$ MeV. Experimental data were taken from Refs. [56] and [55]. The dashed line denotes the polarization and cross-section data uncorrected for the CN contribution.

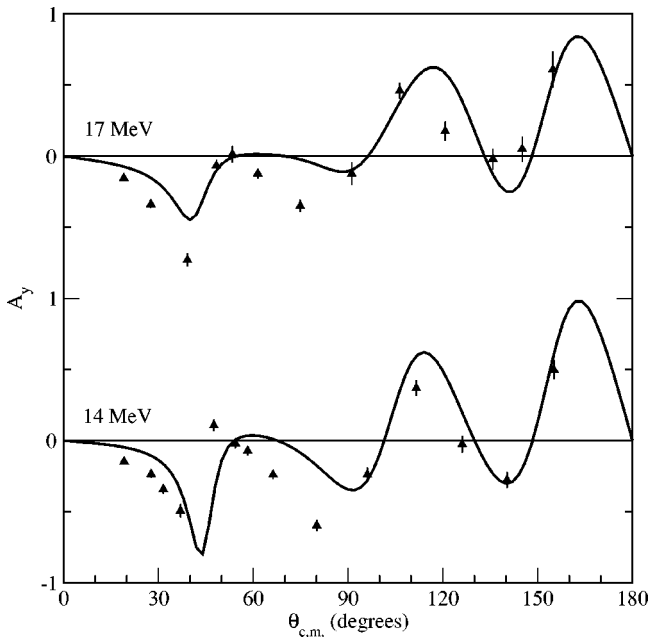

FIG. 10. The $A_y(\theta)$ data (solid line) at $E_n = 14$ and 17 MeV. Experimental data were taken from Martin and Walter [62].

excellent agreement with these data.

The σ_T relativistic DOM fit is compared with the total cross-section data, and with calculations using phenomenological potentials, in Figs. 7 and 8. It should be stressed that only the experimental total cross-section data of Refs. [34,35], shown as empty circles in Fig. 7, were used in the DOM parameter search. In Fig. 7, the total cross-section fit is in excellent agreement with the experimental data in the whole energy range from 10 to 250 MeV. The only phenomenological potential which gives a comparable agreement with experimental data up to 200 MeV is the one by Koning and Delaroche [41], slightly larger than data in the region of the cross section maximum. The Madland OMP overestimated the experimental cross section by almost 20% above 100 MeV. The σ_T relativistic DOM fit is compared to the high-resolution total cross section data, measured by Ohkubo [73] and Rohr *et al*. [74], in Fig. 8. The total cross-section fit using the relativistic DOM potential is in good agreement with the averaged experimental data in the whole energy range from 0.1 to 10 MeV, and is practically equal to the cross section derived from phenomenological OMP by Koning and Delaroche [41]. The total cross section calculated by the phenomenological potential of Petler *et al.* [38] is smaller than the one calculated by the relativistic DOM potential of the present work in the whole energy range from 0.1 to 10 MeV, but the shape remains quite similar for all compared total cross-section calculations. A calculation using the relativistic DOM potential, including reorientation effects by considering Al as a deformed nucleus ($\beta = 0.4$) with a ground-state spin equal 2.5, is shown by the dashed line in Fig. 8. This calculation was carried out without readjusting any potential parameter to see the effect of deformation on the total cross section. The maximum energy in this calcula-

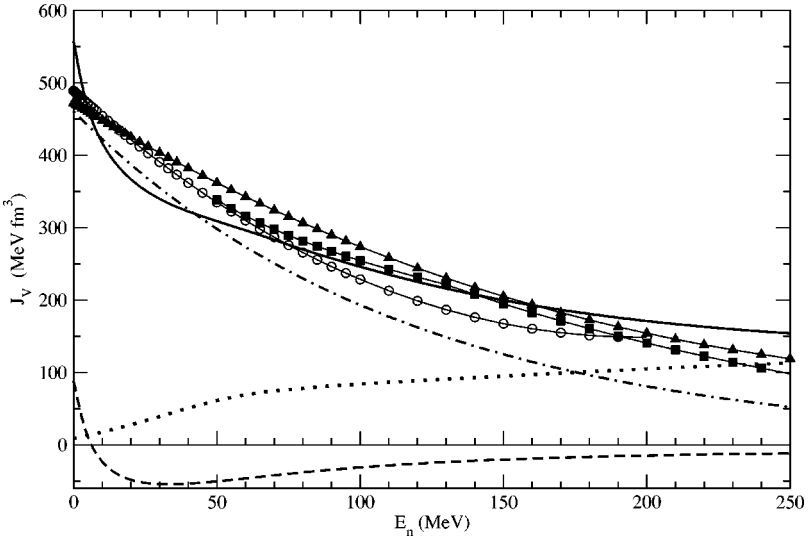

FIG. 11. Energy dependence of the volume integrals per nucleon of the Hartree-Fock (dot-dashed line), volume (dotted line), and surface (dashed line) dispersive components of the real part of the $n+{}^{27}$Al mean field. The thick solid curve represents the sum of all contributions. Nonlocality was considered in the volume imaginary potential. The solid squares, solid triangles, and empty circles connected by lines were obtained from the phenomenological OMP from Refs. [39], [40], and [41], respectively.

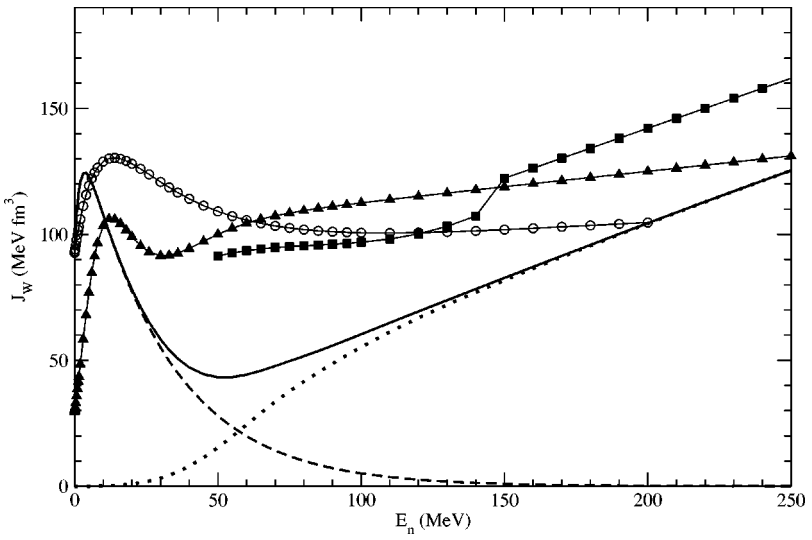

FIG. 12. Energy dependence of the volume integrals per nucleon of the volume (dotted line) and surface-peaked (dashed line) components of the imaginary part of the $n+{}^{27}$Al mean field. The solid curve represents the sum of all contributions. Nonlocality was considered in the volume imaginary potential. The solid squares, solid triangles, and empty circles connected by lines were obtained from the phenomenological OMP from Refs. [39], [40], and [41], respectively.

tion was equal to the energy of the first excited level, to avoid complexity linked to the coupled channel approach. We can see that reorientation effects lead to a reduction of the calculated cross section by 10% from 0.1 to 0.8 MeV. The small differences between the solid and dashed curves are a measure of the error incurred by the neglect of reorientation effects and nuclear deformation.

Figure 9 shows the comparison between the experimental analyzing power and differential cross section at 7.5–7.6 MeV and the predictions of our relativistic DOM. The agreement is good in view of the fact that polarization data were not used in our fitting procedure. It can be seen that the CN contribution is still quite important at this energy. Polarization measurements at 14 and 17 MeV are compared with DOM calculations in Fig. 10.

The average volume integral for the real part of the optical potential was determined for the relativistic DOM potential as well as for the available phenomenological potentials, and is shown in Fig. 11. In the same figure the ''Hartree-Fock,'' volume, and surface dispersive contributions are shown. The largest difference between our DOM potential and the phenomenological potentials is located below 50 MeV, where the surface dispersive contribution reaches a minimum and then changes its sign, becoming positive. This pure dispersive effect cannot be simulated by any variation of the phenomenological OMP parameters. It is interesting that the real volume integral above 200 MeV is dominated by the dispersive volume contribution as a result of the nonlocality.

The average volume integral for the imaginary part of the optical potential was also calculated. In this case there are large differences between phenomenological potentials and DOM results, as can be seen in Fig. 12. The low-energy behavior is different, as was the case for the real volume integral, because of the dominance of the dispersive contribution. However, the high-energy region is also quite different. The DOM integral increases with energy as a result of the nonlocality contribution to the volume absorptive potential. The only phenomenological potential showing a similar behavior is the Madland OMP [39]. Its imaginary volume integral is parallel to the integral calculated using the relativistic DOM potential (not considering a discontinuity caused

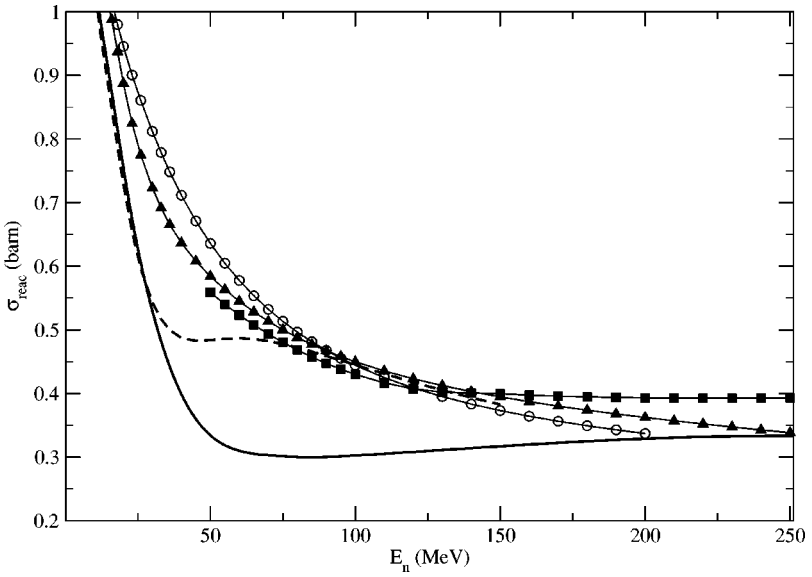

FIG. 13. Energy dependence of the $n+{}^{27}$Al reaction cross section from 0 up to 250 MeV. The thick solid and dashed curves have been calculated using the relativistic and nonrelativistic DOM potentials of the present work. The solid squares, solid triangles, and empty circles connected by lines were obtained from the phenomenological OMP by Madland [39], Lee *et al.* [40], and Koning and Delaroche [41], respectively, in their range of validity.

by two different functional forms employed for reduced radius by Madland; one below 140 MeV, and a second above this value). There is a clear connection between this increase of the imaginary volume integral and the saturation of the reaction cross section at energies above 125 MeV, as shown in Fig. 13. This behavior is consistent with the semiclassical estimation of the reaction cross section. The relativistic DOM potential reaction cross section reaches a near constant value of 0.3 barn. The asymptotical estimate of the reaction cross section is πR^2, equivalent to the reduced radius of 1.03 fm. This value compares well with the averaged reduced radius of 1.1–1.2 fm used for the imaginary potential geometry of the DOM potential. It is interesting to point out that different reaction cross sections will have direct impacts on cross sections available for any statistical model calculations.

IV. CONCLUSIONS

In this work we have presented a dispersive relativistic spherical optical model analysis of neutron scattering up to 250 MeV for an ^{27}Al nucleus. The excellent overall agreement obtained between predictions and experimental data would not have been possible without including dispersive terms in the calculations and nonlocality effects in the volume absorptive potential. High-precision scattering measurements for aluminum above 30 MeV are necessary to establish our analysis on firmer grounds and to confirm our present results.

ACKNOWLEDGMENTS

This work was supported by Junta de Andalucía and the Spanish CICYT under Contract No. PB1998-1111 and by the European Union under Contract No. FIKW-CT-2000-00107. One of the authors (R.C.) acknowledges support from the Ministerio de Educación, Deportes y Cultura de España, Secretaría de Estado de Educación y Universidades.

[1] C. Mahaux and H. Ngo, Nucl. Phys. **A431**, 486 (1984).
[2] C. Mahaux and R. Sartor, Nucl. Phys. **A468**, 193 (1987).
[3] C.H. Johnson, D.J. Horen, and C. Mahaux, Phys. Rev. C **36**, 2252 (1987).
[4] C. Mahaux and R. Sartor, Nucl. Phys. **A528**, 253 (1991).
[5] *Advances in Nuclear Physics*, edited by J. W. Negele and E. Vogt (Plenum, New York, 1991), p. 1991.
[6] M.A. Nagarajan, C. Mahaux, and G.R. Satchler, Phys. Rev. Lett. **54**, 1136 (1985).
[7] C. Mahaux, H. Ngo, and G.R. Satchler, Nucl. Phys. **A449**, 354 (1986).
[8] M. Lozano, Phys. Rev. C **36**, 452 (1987).
[9] Y. Wang, C.C. Foster, E.J. Stephenson, L. Yuan, and J. Rapaport, Phys. Rev. C **45**, 2891 (1992).
[10] C. H. Dasso, R. J. Liotta, and M. Lozano, Phys. Rev. C **54**, 1217 (1996).
[11] G. Passatore, Nucl. Phys. **A95**, 694 (1967).
[12] R. Lipperheide and A.K. Schmidt, Nucl. Phys. **A112**, 65 (1968).
[13] C. Mahaux and R. Sartor, Nucl. Phys. **A484**, 205 (1988).
[14] C. Mahaux and R. Sartor, Nucl. Phys. **A493**, 157 (1989).
[15] C.H. Johnson and C. Mahaux, Phys. Rev. C **38**, 2589 (1988).
[16] W. Tornow, Z.P. Chen, and J.P. Delaroche, Phys. Rev. C **42**, 693 (1990).
[17] J.P. Delaroche, Y. Wang, and J. Rapaport, Phys. Rev. C **39**, 391 (1989).
[18] S. Chiba, P.T. Guenter, A.B. Smith, M. Sugimoto, and R.D. Lawson, Phys. Rev. C **45**, 1260 (1992).
[19] Y. Wang, C.C. Foster, R.D. Polak, J. Rapaport, and E.J. Stephenson, Phys. Rev. C **47**, 2677 (1993).
[20] C. Mahaux and R. Sartor, Nucl. Phys. **A568**, 1 (1994).
[21] R.W. Finlay, J. Wierzbicki, R.K. Das, and F.S. Dietrich, Phys. Rev. C **39**, 804 (1989).
[22] G.J. Weisel, W. Tornow, C.R. Howell, P.D. Felsher, M. AlOhali, M.L. Roberts, R.K. Das, R.L. Walter, and G. Mertens, Phys. Rev. C **54**, 2410 (1996).
[23] X.X. Zhang, Z. Chen, Y. Chen, J. Yuan, G. Tang, G. Zhang, J. Chen, Yu.M. Gledenov, G. Kluukhenkhuu, and M. Sedysheva, Phys. Rev. C **61**, 054607 (2000).
[24] R.D. Lawson, P.T. Guenther, and A.B. Smith, Nucl. Phys. **A493**, 267 (1989).
[25] C.H. Johnson, R.F. Carlton, and R.R. Winters, Phys. Rev. C **39**, 415 (1989).
[26] C. Mahaux and R. Sartor, Phys. Rev. C **36**, 1777 (1987).
[27] A.B. Smith, P.T. Guenther, and R.D. Lawson, Nucl. Phys. **A455**, 344 (1986).
[28] S. Chiba, P.T. Guenter, R.D. Lawson, and A.B. Smith, Phys. Rev. C **42**, 2487 (1990).
[29] R.K. Das and R.W. Finlay, Phys. Rev. C **42**, 1013 (1990).
[30] G.J. Weisel and R.L. Walter, Phys. Rev. C **59**, 1189 (1999).
[31] M. M. Nagadi, J. P. Delaroche, C. R. Howell, W. Tornow, and R. L. Walter, ''The dispersive optical model for $n+^{27}$Al.'' Technical Report No. TUNL-XXIX Triangle University Nuclear Laboratory, 1990, p. 87.
[32] E.A. Romanovsky, H.A. Hussein, and R.I. Bogdanov, Izv. Akad. Nauk SSSR, Ser. Fiz. **53**, 156 (1989).
[33] E.A. Romanovsky and T.I. Spasskaya, Izv. Akad. Nauk SSSR, Ser. Fiz. **59**, 136 (1995).
[34] R. W. Finlay, F. Fink, W. Abfalterer, P. Lisowski, G. L. Morgan, and R. C. Haight, in *Proceedings of the Nuclear Data for Science and Technology Conference, Julich, 1991*, edited by S. M. Qaim (Springer-Verlag, Berlin, 1992), p. 720.
[35] R.W. Finlay, W. Abfalterer, F. Fink, E. Montei, T. Adami, P. Lisowski, G.L. Morgan, and R.C. Haight, Phys. Rev. C **47**, 237 (1993).
[36] A.J. Koning, J.P. Delaroche, and O. Bersillon, Nucl. Instrum. Methods Phys. Res. A **414**, 49 (1998).
[37] M.B. Chadwick *et al.*, Nucl. Sci. Eng. **1331**, 293 (1999).
[38] J.S. Petler, M.S. Islam, R.W. Finlay, and F.S. Dietrich, Phys. Rev. C **32**, 673 (1985).
[39] D. G. Madland, in *Proceedings of the Specialists' Meeting on*

Preequilibrium Nuclear Reactions. Semmering, Austria, 1988, edited by B. Strohmaier, Nuclear Energy Agency Nuclear Data Committee Report No- NEANDC-245 'U', Paris 1988, p. 103.
[40] Y.O. Lee, J. Chang, T. Fukahori, and S. Chiba, J. Nucl. Sci. Technol. **36**, 1125 (1999).
[41] A. Koning and J. P. Delaroche (unpublished).
[42] A. Nadasen, P. Schwandt, W.W. Jacobs, A.D. Bacher, P.T. Debevec, M.D. Kaitchuck, and J.T. Meek, Phys. Rev. C **23**, 1023 (1981).
[43] C.S. Whisnant, J.H. Dave, and C.R. Gould. Phys. Rev. C **30**, 1435 (1984).
[44] R. Lipperheide, Z. Phys. **202**, 58 (1967).
[45] G.E. Brown and M. Rho, Nucl. Phys. **A372**, 397 (1981).
[46] *Handbook for Calculations of Nuclear Reaction Data: Reference Input Parameter Library* (IAEA, Vienna, Austria, 1998).
[47] C. Mahaux and R. Sartor, Nucl. Phys. **A458**, 25 (1986).
[48] J.M. van der Kam, G.J. Weisel, and W. Tornow, J. Phys. G **26**, 1787 (2000).
[49] J. Raynal, ''Optical model and coupled-channels calculations in nuclear physics,'' in *Computing as a language of physics, ICTP International Seminar Course, Trieste, Italy, 1971* (IAEA, Vienna, Austria, 1972), p. 281.
[50] J. Raynal, program ECIS95.
[51] T. Kawano, program COH.
[52] R. Capote, A. Molina, and J.M. Quesada, J. Phys. G **27**, B15 (2001).
[53] J.H. Towle and W.B. Gilboy, Nucl. Phys. **39**, 300 (1962).
[54] S. Tanaka, K. Tsukada, M. Maruyama, and Y. Tomita (unpublished).
[55] W. E. Kinney and F. G. Perey, Technical Report No. ORNL-4516, Oak Ridge National Laboratory, 1976.
[56] G. Dagge, W. Grumm, J.W. Hammer, K.-W. Hoffmann, and G. Schreder, Phys. Rev. C **39**, 1768 (1989).
[57] D.E. Velkley, D.W. Glasgow, M.T. Brandenberger, J.D. McEllistrem, J.C. Manthuruthil, and C.P. Poirier, Phys. Rev. C **9**, 2181 (1974).
[58] G. Boerker, R. Boettger, H. J. Brede, H. Klein, W. Mannhart, and R. L. Siebert, Conference on Nuclear Data for Science and Technology, Mito, Japan, 1988 (http://www.nndc.bnl.gov/nndc/exfor/, EXFOR 22113)
[59] A. Bratenahl, S. Fernbach, R.H. Hildebrand, C.E. Leith, and B.J. Moyer, Phys. Rev. **77**, 597 (1950).
[60] G.L. Salmon, Nucl. Phys. **21**, 15 (1960).
[61] C.P. Van Zyl, R.G.P. Voss, and R. Wilson, Philos. Mag. **1**, 1003 (1956).
[62] Ph. Martin and R.L. Walter, Phys. Rev. C **34**, 384 (1986).
[63] J. de Juren and B.J. Moyer, Phys. Rev. **81**, 919 (1951).
[64] A.E. Taylor and E. Wood, Philos. Mag. **44**, 95 (1953).
[65] P.H. Bowen, J.P. Scanlon, G.H. Stafford, J.J. Thresher, and P.E. Hodgson, Nucl. Phys. **22**, 640 (1961).
[66] D.F. Measday and J.N. Palmieri, Nucl. Phys. **85**, 129 (1966).
[67] R.J. Schneider and A.M. Cormack, Nucl. Phys. **119**, 197 (1968).
[68] S. Cierjaks, P. Forti, D. Kopsch, L. Kropp, J. Nebe, and H. Unseld, Technical report, Kernforschungszentrum Karlsruhe Report Nos. KFK-1000, EUR-3963E, and EANDC(E)-111, 1968.
[69] D.G. Foster, Jr. and D.W. Glasgow, Phys. Rev. C **3**, 576 (1971).
[70] F. G. Perey, T. A. Love, and W. E. Kinney, ''A test of neutron total cross-section evaluations from 0.2 to 20 MeV for C, O, Al, Si, Ca and SiO_2,'' Technical Report No. ORNL-4823, Oak Ridge National Laboratory, 1972.
[71] D. C. Larson, J. A. Harvey, and N. W. Hill, ''Measurement of neutron total cross sections at ORELA to 80 MeV,'' Technical Report No. ORNL-5787, Oak Ridge National Laboratory, 1981, p. 174.
[72] J. Franz, H.P. Grotz, L. Lehmann, E. Roessle, H. Schmitt, and L. Schmitts, Nucl. Phys. **A490**, 667 (1988).
[73] M. Ohkubo, Proceedings of the International Conference on Nuclear Data for Basic and Applied Science, Santa Fe, New Mexico, 1985 (http://www.nndc.bnl.gov/nndc/exfor/, EXFOR 21926)
[74] G. Rohr, R. Shelley, C. Nazareth, and M. Moxon, Conference on Nuclear Data for Science and Technology, Gatlinburg, Tennessee, 1994 (http://www.nndc.bnl.gov/nndc/exfor/, EXFOR 22331)
[75] R. B. Schwartz, R. A. Schrack, and H. T. Heaton, Technical Report No. NBS-MONO-138, National Bureau of Standards, 1974.
[76] W. Hauser and H. Feshbach, Phys. Rev. **87**, 366 (1952).
[77] P.A. Moldauer, Nucl. Phys. **A344**, 185 (1980).
[78] F.G. Perey, Phys. Rev. **131**, 745 (1963).
[79] E. D. Arthur and P. G. Young, in *Proceedings of the Symposium on Neutron Cross Sections from 10 to 50 MeV. Brookhaven National Laboratory, Upton, NY*, edited by M. R. Bhat and S. Pearlstein, Brookhaven National Laboratory Report No. BNL-NCS-51245, (BNL, New York, 1980), Vol. II, p. 731.
[80] O. F. Lemos, Technical Report, Orsay, Series A No. 136, 1976.
[81] A. Gilbert and A.G.W. Cameron, Can. J. Phys. **43**, 1446 (1965).
[82] R.C. Harper and W.L. Alford, J. Phys. G **8**, 153 (1982).